Available online at www.sciencedirect.com

SciVerse ScienceDirect

Geochimica et Cosmochimica Acta 80 (2012) 108–124

Geochimica et Cosmochimica Acta

www.elsevier.com/locate/gca

The speciation of marine particulate iron adjacent to active and passive continental margins

Phoebe J. Lam [a,*], Daniel C. Ohnemus [a,b], Matthew A. Marcus [c]

[a] Department of Marine Chemistry and Geochemistry, Woods Hole Oceanographic Institution, Woods Hole, MA 02543, United States
[b] MIT-WHOI Joint Program in Oceanography, United States
[c] Advanced Light Source, Lawrence Berkeley National Laboratory, Berkeley, CA 94720, United States

Received 2 May 2011; accepted in revised form 28 November 2011

Abstract

We use synchrotron-based chemical-species mapping techniques to compare the speciation of suspended (1–51 μm) marine particulate iron collected in two open ocean environments adjacent to active and passive continental margins. Chemical-species mapping provides speciation information for heterogeneous environmental samples, and is especially good for detecting spectroscopically distinct trace minerals and species that could not be detectable by other methods. The average oxidation state of marine particulate iron determined by chemical-species mapping is comparable to that determined by standard bulk X-ray Absorption Near Edge Structure spectroscopy. Using chemical-species mapping, we find that up to 43% of particulate Fe in the Northwest Pacific at the depth of the adjacent active continental margin is in the Fe(II) state, with the balance Fe(III). In contrast, particulate iron in the eastern tropical North Atlantic, which receives the highest dust deposition on Earth and is adjacent to a passive margin, is dominated by weathered and oxidized Fe compounds, with Fe(III) contributing 90% of total iron. The balance is composed primarily of Fe(II)-containing species, but we detected individual pyrite particles in some samples within an oxygen minimum zone in the upper thermocline. Several lines of evidence point to the adjacent Mauritanian continental shelf as the source of pyrite to the water column. The speciation of suspended marine particulate iron reflects the mineralogy of iron from the adjacent continental margins. Since the solubility of particulate iron has been shown to be a function of its speciation, this may have implications for the bioavailability of particulate iron adjacent to passive compared to active continental margins.

1. INTRODUCTION

Iron is the most important micronutrient for primary production in the ocean (Boyd and Ellwood, 2010). Despite being one of the more abundant elements on Earth, iron has a very low solubility in the oxic conditions of the ocean, and thus limits marine primary production in many regions. Particulate iron is often a large component of total iron in the ocean, and has the potential to be a source of dissolved iron. Typical solubilities of Fe from natural aerosol particles range from less than 1% up to 26% of total Fe (Sedwick et al., 2007; Buck et al., 2010), with its solubility a function of the source region of the aerosol (Sholkovitz et al., 2009). Experiments on putative source minerals for aerosols have shown that the solubility of Fe is a function of the mineralogy of Fe (Journet et al., 2008; Schroth et al., 2009). Similarly, the bioavailability of colloidal and particulate iron to phytoplankton in culture depends on its speciation (Rich and Morel, 1990; Wells et al., 1991; Nodwell and Price, 2001). These data suggest that the degree to which marine particulate iron may be a source of dissolved or bioavailable iron is likely a function of its mineralogy and speciation.

Continental margins have increasingly been viewed as a source of both dissolved (Elrod et al., 2004; Moore and

* Corresponding author. Address: Department of Marine Chemistry and Geochemistry, Woods Hole Oceanographic Institution, MS #25, 266 Woods Hole Rd., MA 02543, United States. Tel.: +1 508 289 3792; fax: +1 508 457 2193.
E-mail address: pjlam@whoi.edu (P.J. Lam).

0016-7037/$ - see front matter © 2011 Elsevier Ltd. All rights reserved.
doi:10.1016/j.gca.2011.11.044

Braucher, 2008; Tagliabue et al., 2009) and particulate (Lam et al., 2006; Lam and Bishop, 2008) iron to the open ocean. Two broad classifications of continental margins exist: active margins that surround the Pacific, and passive margins that surround the Atlantic and elsewhere. Active margins are located at the edges of converging lithospheric plates, are associated with mountain building processes such as earthquakes and active volcanoes, and are characterized by narrow continental shelves and steeper continental slopes (Seibold and Berger, 1993). Passive margins are steadily sinking regions generally characterized by broad, flat shelves, often with thick sedimentary accumulations. Here, we examine whether the type of margin affects the speciation of particulate iron that is transported to the open ocean.

Despite advances in Fe speciation in the dissolved phase, very little is known about the composition of particulate iron. Existing knowledge is based on the application of chemical leaches of varying strengths (Landing and Bruland, 1987; Poulton and Raiswell, 2005; Berger et al., 2008; Raiswell et al., 2010), or estimates of lithogenic composition from crustal ratios of elemental abundance (Frew et al., 2006), both of which provide a useful but necessarily operationally defined view of particulate iron speciation. Furthermore, operational definitions vary widely between papers, so the "lithogenic" fraction in one study determined using a Fe:Al ratio (Frew et al., 2006) may have a different meaning than the "lithogenic" fraction in a different study determined as the residual from an acetic acid leach (Landing and Bruland, 1987) or simply as total inorganic particulate Fe (Boyd et al., 2010).

Synchrotron-based X-ray absorption spectroscopic techniques such as X-ray Absorption Near Edge Structure (XANES) and Extended X-ray Absorption Fine Structure (EXAFS) analyses can provide information about the oxidation state, mineralogy, and nearest-neighbor bonding distances of many elements including iron in heterogeneous environmental samples (Brown and Sturchio, 2002; Manceau et al., 2002). XANES and EXAFS can be done on "bulk" beamlines that determine the average Fe speciation of a sample at the expense of minor species (Lam and Bishop, 2008; Schroth et al., 2009), or on micro-focused beamlines to examine the speciation of single iron particles in detail (Lam et al., 2006). EXAFS spectroscopy is more appropriate for distinguishing between compounds within a group, especially for difficult-to-distinguish weakly crystalline Fe(III) species (Schroth et al., 2009; Toner et al., 2009b). With typical EXAFS data collection times of up to 8 h per particle compared to less than 20 min for XANES, EXAFS is not an appropriate technique for obtaining a representative view of the speciation of marine particulate iron particles. The power of XANES lies in the greater number of spectra that can be collected quickly and its ability to identify some crystalline minerals, especially when XANES collection is extended into the EXAFS region. The challenge with microprobe spectroscopy comes in balancing the depth of information obtained from single particle analysis with the competing need for collecting data from enough particles to create a representative picture of the chemical composition of a sample.

Here we describe the application of a chemical species mapping technique for determining the speciation of marine particulate iron. Chemical-species mapping is a microprobe technique that combines the spatial information provided by microfocused X-ray fluorescence (XRF) mapping with chemical information gleaned from single particle XANES to allow a rapid and statistically meaningful assessment of the speciation of marine particulate iron. We show that chemical-species mapping yields results for the average fraction of Fe(II) that are comparable to those obtained from bulk spectroscopy, but also provides information about the spatial distribution of species. In addition, chemical-species mapping can be used to detect species which include a small minority of the overall Fe but which are locally concentrated in micron-scale spots. This technique has been applied successfully to quantify the spatial distribution of oxidation state of Se in plants (Pickering et al., 2000) and sediments (Sutton et al., 1995; Oram et al., 2008), Cr in ore processing residue (Chrysochoou et al., 2009), and Fe in interplanetary dust particles (Marcus, 2010; Ogliore et al., 2010). To our knowledge, chemical-species mapping has not been applied to the problem of marine particulate iron.

2. METHODS

2.1. Sample collection

Depth profiles of suspended marine particulate samples were collected using McLane in situ pumps during the Sources of IRon to the Eastern tropical North Atlantic (SIRENA) cruise on the *R/V Oceanus* (OC449-3) in the eastern tropical North Atlantic in September 2008 at five stations along an open ocean to coastal transect (Fig. 1a, Table 1). Station 1 furthest from shore was at the site of the Tropical Eastern North Atlantic Time Series Observatory (TENATSO) station, and station 6 closest to shore was in Mauritanian upwelling waters. There were no particles collected at station 5. Eleven pumps were clamped onto a 700 m non-metallic wire (Hytrel-coated Vectran) to collect depth profiles of size-fractionated marine particulate samples. Particulate samples were collected on the standard filter suite used for large volume in situ filtration (Bishop and Wood, 2008): paired quartz fiber filters (Whatman QMA) of 1 μm nominal pore size overlain by a 51 μm polyester filter in a 142 mm filter holder manufactured by McLane. While the QMA filter has a relatively coarse nominal pore size, it has far superior flow and particle distribution characteristics compared to smaller pore-size "high-flow" plastic filters such as polyethersulfone. All filters were acid leached in 10% HCl prior to use. Immediately upon collection, filters were lightly misted with ultrapure deionized water under vacuum to reduce salt from residual seawater, photographed, and dried at 60 °C overnight in a clean oven dedicated to drying suspended marine particles. Oven drying was required to preserve the particulate organic carbon in our suspended marine particulate samples, but likely led to some aging of Fe(III) species (Raiswell et al., 2010) (Schwertmann and Cornell, 2000). All filter processing and drying was conducted in a HEPA-filtered clean environment.

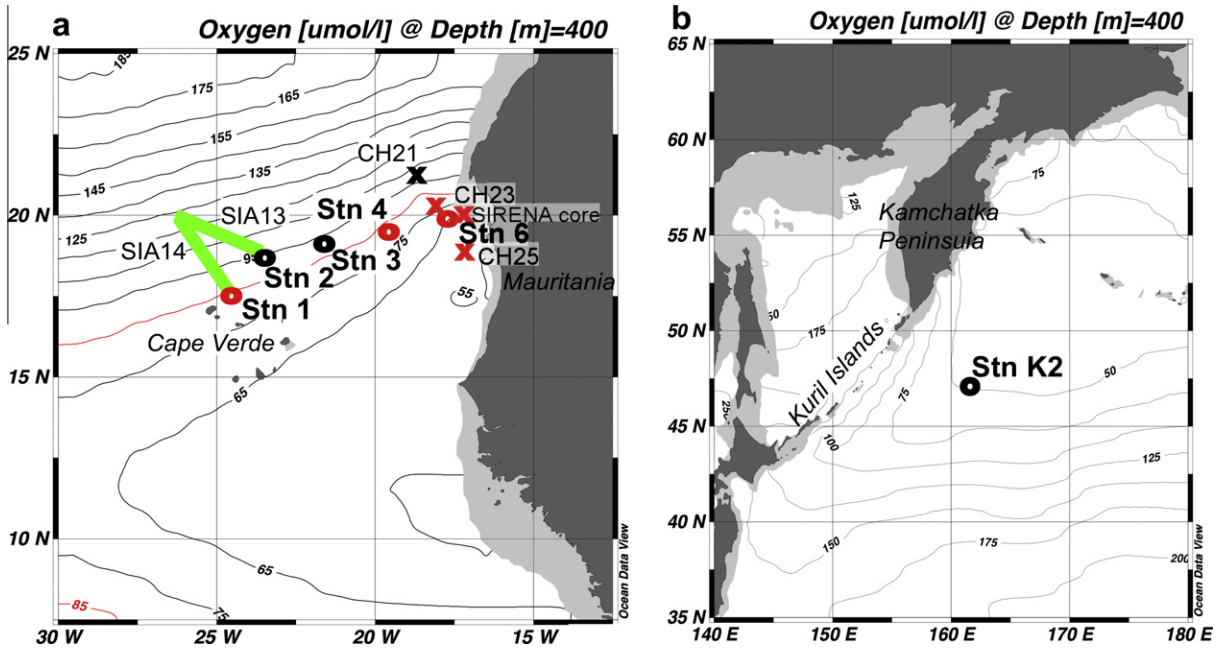

Fig. 1. Maps of sample locations from (a) the eastern tropical North Atlantic, and (b) the Northwest Pacific, overlaid on objectively analyzed dissolved oxygen concentrations at 400 m from the 2009 World Ocean Atlas. Contour lines are every 10 μmol O_2/L for (a) and every 25 μmol O_2/L for (b). In-situ pumping station locations (o), sediment core sites (x), and aerosol collection transits (green bars) marked. For the eastern tropical North Atlantic, water column and sediment samples containing pyrite are plotted in red, and are located within the 85 μmol/L dissolved oxygen contour line. Aerosol sample SIA7c was collected to the west of the map area. (For interpretation of the references to color in this figure legend, the reader is referred to the web version of this article.)

Typical volumes filtered were about 1000 L over a 133 cm^2 active filter area, resulting in a particle loading that is approximately four times that of filtration from a typical 10 L GO-Flo bottle onto a 25 mm filter. Here we report particulate data from the suspended (1–51 μm) size fraction only. We also report X-ray data from 1–51 μm suspended particulate samples collected previously from station K2 at 47°N, 161°E in the Northwest Pacific (Fig. 1b, Table 1). Sample collection details for K2 samples are reported in (Bishop and Wood, 2008); sample processing and storage procedures were identical.

Sediment and aerosol samples were also collected during the SIRENA cruise as putative endmember sources of marine particulate iron. A sediment sample ("SIRENA core") from the upper slope (313 m) of the Mauritanian continental margin was collected using a gravity corer (Fig. 1a, Table 1). Sediment from the uppermost part of the core was frozen upon collection and freeze dried on land for analysis at the synchrotron. Because gravity corers disrupt the sediment–water interface, this material does not represent true core-top. We also obtained three subsamples of true core-top sediments ("CH21", "CH23", "CH25") collected using a multi-corer along the continental slope (1000–2500 m) on a previous cruise (OC437-7) to the area in July 2007 (Fig. 1a, Table 1).

Aerosol samples were collected when the ship was in transit using a sector-controlled aerosol sampler mounted on the forward railing of the 02 deck of the Oceanus. Samples were collected on acid-leached, pre-weighed 47 mm 0.4 μm polycarbonate membrane filters (Nuclepore). Air was filtered only when the wind speed was greater than 5 m/s and originated from the forward-pointing 180° of the ship. Filters were changed after 40–100 m^3 of air was filtered. Here we analyze three aerosol samples ("SIA7C", "SIA13C", "SIA14C") collected on OC449-2, the leg immediately prior to SIRENA, when the prevailing wind direction was from the northeast and a fine coating of orange Sarahan dust covered the ship. SIA7C was collected southwest of the SIRENA transect (not shown), and SIA13C and SIA14C were collected just northwest of SIRENA stations 1 and 2 (Fig. 1; Table 1).

Appropriate process blanks were collected for marine particulate and aerosol samples. Blanks for marine particulates were QMA filters that had been exposed to filtered seawater and processed identically to regular samples. Aerosol blanks were polycarbonate filters that were loaded into filter holders with no pump connected.

2.2. Analytical methods

Subsamples of the top QMA filter (1–51 μm size fraction) representing an equivalent of 20–25 L filtered seawater were leached in 0.6 N HCl at 60 °C overnight (12–16 h). This operational leach was used to be consistent with previous acid-leachable particulate Fe data from the Subarctic Pacific (Lam et al., 2006; Bishop and Wood, 2008; Lam and Bishop, 2008). The leachate was filtered and diluted to 0.06 N (1%) HCl and analyzed on an Element2 high resolution Inductively Coupled Plasma Mass Spectrometer (ICP-MS) with a Quartz spray chamber

Table 1
Locations and dates of sample collection. For suspended particulate matter, the inventory of Fe species and total Fe in the upper 500 m for each station are listed. HCl Fe is acid-leachable Fe determined by ICP-MS (see Section 2.2). Other Fe species are determined by chemical-species mapping.

Station	Cruise#	Latitude (°N)	Longitude (°E)	Date	Water depth	Distance from coast (km)	HCl Fe inventory (mmol m^{-2})	Fe(II) inventory (mmol m^{-2})	Fe(III) inventory (mmol m^{-2})	Total Fe inventory (mmol m^{-2})	Pyrite inventory (mmol m^{-2})
Suspended particulate matter											
Stn 1	OC449-3	17.40	−24.50	09/09/08	3525	900	3.90	0.63	5.72	6.36	9.88e-5
Stn 2	OC449-3	18.50	−23.40	09/10/08	3700	750	4.25	0.79	6.36	7.15	0
Stn 3	OC449-3	18.99	−21.51	09/11/08	3300	550	3.62	0.38	6.74	7.09	0
Stn 4	OC449-3	19.39	−19.60	09/12/08	3250	345	8.04	0.69	9.55	10.24	1.24e-2
Stn 6	OC449-3	19.85	−17.70	09/14/08	1330	140	13.67	1.00	15.02	16.00	5. 03e-2
Stn K2	RR_K2	47.00	161.00	07/31/05	5280	550	2.07	0.95	1.68	2.63	0
Sediments											
Stn 5	OC449-3	19.88	−17.45	09/13/08	313						
CH21	OC437-7	21.15	−18.60	07/19/07	2765						
CH23	OC437-7	19.95	−17.87	07/19/07	1442						
CH25	OC437-7	18.65	−17.32	07/21/07	2274						
Aerosols					Volume filtered (m^3)						
SIA7C-start	OC449-2	10.55	−35.09	08/18/08							
SIA7C-stop	OC449-2	15.58	−30.55	08/21/08	100.0						
SIA13C-start	OC449-2	18.53	−23.42	09/01/08							
SIA13C-stop	OC449-2	19.93	−26.51	09/02/08	43.4						
SIA14C-start	OC449-2	19.93	−26.61	09/02/08							
SIA14C-stop	OC449-2	17.40	−24.51	09/03/08	46.2						

introduction system to determine the concentrations of acid-leachable Fe. Mixed element external standards in 1% HCl were used to determine calibration curves, and an internal standard of 0.5 ppb In was used to correct for instrument drift.

2.3. XRF data acquisition for chemical-species mapping (Fe speciation) analysis

Six or seven depths from each 11-point suspended marine particle profile from SIRENA and station K2 were chosen for XRF chemical-species mapping using acid-leachable Fe concentrations determined from ICP-MS as a guide to resolve key features in the profiles. All samples (marine particles, aerosol, and sediment samples) were mounted dry and at ambient atmosphere for analysis at microprobe beamline 10.3.2 at the Advanced Light Source (Marcus et al., 2004). Sediment samples were mounted without further size fractionation, and thus have a different particle size spectrum than is found in the water column particles samples. A randomly chosen 500 μm × 500 μm area was typically mapped using a beam spot size of 5 μm, a dwell time of 100 ms, and a pixel size of 4 μm. The mapping area represented an equivalent volume filtered of 10–20 mL for the eastern tropical North Atlantic samples, and 20–40 mL for the Northwest Pacific samples. Data reported here were collected in January, March, and July 2010. The absolute energy of the monochromator was calibrated using an Fe foil (Fe K-edge at 7110.75 eV) at the beginning of each run and periodically throughout the run. Typically, counts in 10 spectral regions of interest were recorded for each map, including CaKα (3510–3850 eV), CrKα (5260–5660 eV), and FeKα (6150–6690 eV). The distance of the seven-element Ge solid-state detector relative to the sample was adjusted for optimal counts. XRF data for chemical-species maps were collected from blank filters or substrates for each sample type and at each detector position used for samples. Companion maps of an XRF thin film standard (Micromatter™, Vancouver, Canada) for Fe (43.9 μg Fe/cm^2) were collected at 7180 eV for each detector position and incident beam configuration to quantify total Fe concentrations in samples. For comparison, blank corrected Fe loadings on all sample types ranged from 0.1–5.5 μg Fe/cm^2.

Iron sulfides, Fe(II)-containing species (silicates, carbonates, and oxides), and Fe(III) species (silicates and oxides) are easily separated on the basis of their spectral features near the K-edge (O'Day et al., 2004; Marcus et al., 2008; Westphal et al., 2009). A representative compound from each of these three groups was chosen as input spectra for calculating chemical-species maps: (1) pyrite to represent Fe sulfides, (2) biotite to represent Fe(II)-containing species, and (3) 2-line ferrihydrite to represent Fe(III) species (Fig. 2a). These three model compounds were chosen because they appeared frequently in linear combination fits of XANES spectra of marine sediments and suspended particles, and also have distinct spectral features relative to one another. Chemical-species maps generated using input spectra from averages of the most common pyrite-like, biotite-like, and ferrihydrite-like spectra from the marine samples gave very similar results.

The selection of energies used for chemical-species mapping was fine-tuned using an error minimization and analysis program available at the beamline (Marcus, 2010). Most XRF maps for quantitative chemical-species mapping analyses were acquired at 7105, 7118, 7124, and 7180 eV. Some maps collected in January 2010 were acquired with an intermediate energy of 7117 eV instead of 7118 eV, but errors were similar for both sets of energies. The lowest (7105 eV) and highest (7180 eV) energy maps were selected to determine the background and total counts in the FeKα channel. The intermediate two energies were chosen to maximize the difference in spectral features between the three input components. All XRF maps used to generate chemical-species maps were corrected for detector deadtime and registered to each other to compensate for sample motion between maps using the Ca Kα channel.

Maps of Fe species ("chemical-species maps") were calculated using the three input spectra above and assuming a constant background spectrum. The chemical-species mapping calculation partitions total apparent Fe counts at 7180 eV into four channels: background counts from scatter and other non-Fe sources, Fe sulfides, Fe(II)-containing species, and Fe(III) species.

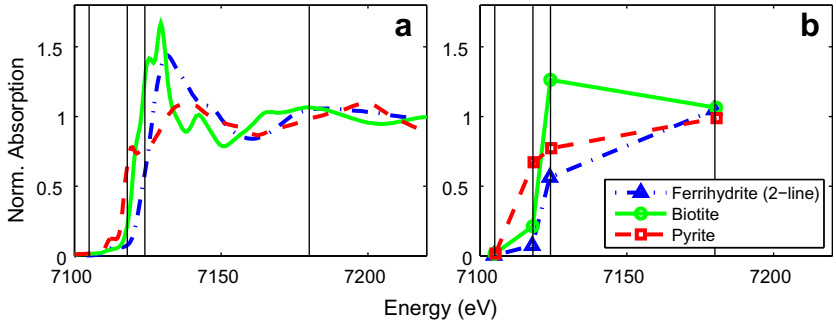

Fig. 2. XANES spectra of the three input compounds to the chemical species map, showing energies at which maps are taken (vertical black lines). (a) Full XANES spectra. (b) Sampled XANES spectra of same input compounds at the 4 mapping energies. Mapping energies were chosen to maximize the difference between the three input compounds.

2.4. Accuracy of Fe species determination from chemical-species maps

The chemical-species mapping procedure in essence takes a 4-point XANES spectrum at each pixel in the map (Fig. 2b), and then fits that spectrum with a linear combination of the 4-point XANES spectra of the three input components (pyrite, biotite, ferrihydrite). We used the error analysis program mentioned earlier to test the accuracy of describing known model compounds using the above energies and input spectra. Sulfides other than pyrite such as pyrrhotite (FeS_{1-x}), whose near-edge structures are slightly different than pyrite, were correctly identified as mostly sulfidic (~90% pyrite-like). We found that many non-sulfidic compounds, especially non-sulfidic Fe(II)-containing species such as volcanic glass, augite and pigeonite (pyroxenes), ilmenite (iron–titanium oxide spinel), and fayalite (olivine) were falsely identified as containing up to 44% pyrite (Table 2). Fe(II) and Fe(III) species were much less frequently falsely identified.

While the chemical species mapping parameters leads to some false positives, this error analysis nonetheless demonstrates that most model compounds are correctly classified into the three groups defined by our method. We calculated an equivalent oxidation state from the fractions of Fe(III), Fe(II), and sulfide attributed to each model compound from the chemical species mapping method, assuming that the Fe(II)-containing species and sulfides had an oxidation state of 2.0, and that Fe(III) species had an oxidation state of 3.0 (Table 2). The equivalent oxidation state from chemical species mapping compared favorably to the expected oxidation state from the chemical formulae as well as to the oxidation state determined from an internally self-calibrating method that relies on spectral features such as the energy difference between the white line and the pre-edge peak (Marcus et al., 2008) (Table 2).

2.5. Identification and quantification of pyrite in marine and aerosol samples

In suspended marine particulate samples, true pyrite particles with compositions verified by XANES spectroscopy were easily identified in the pyrite channel images as small spots with relatively high count rates, and low or no associated counts in the Fe(II) or Fe(III) channels (Fig. 3). In contrast, "false" pyrite particles frequently appeared co-located with Fe(II) and Fe(III) spots that had high count rates. Indeed, over-absorption effects from concentrated Fe spots could be another source of false pyrite: thick or concentrated samples lead to a saturation of the fluorescence response, lowering the apparent energy of the main absorption edge and resulting in an underestimate of the overall valence (Marcus, 2010). Linear combination fitting of a XANES spectrum of one of the spots in the pyrite channel that was co-located with a very bright spot in the Fe(II) channel showed a composition of 18% biotite (Fe(II) mica), 39% akaganeite (Fe(III) oxyhydroxide), and 40% augite (Fe(II) pyroxene) (Fig. 3f). Overabsorption and the presence of augite, one of the minerals that is falsely identified as pyrite by our chemical-species mapping parameters (Table 2), were likely both sources of false pyrite in this particle.

For marine and aerosol samples, most of the counts in the pyrite channel were due to non-sulfidic Fe(II) from overabsorption effects and false attribution of pyrite from certain Fe(II)-containing species. Indiscriminate quantification of all counts from a pyrite map would thus be a significant overestimate of true pyrite, with the error depending on the intensity and identity of the non-sulfidic iron. It is impossible to automatically correct for these sources of error with only information from the chemical species maps. Instead we manually identified all particles appearing in the pyrite channel that were not co-located with intense spots in the Fe(II) or Fe(III) channels. Since the number of pyrite particles identified by these criteria was small, we verified the identities of these spots by XANES. In the example given in Fig. 3, applying these criteria results in the identification of six true pyrite particles out of a total of more than a dozen spots appearing in the pyrite chemical species map for this sample. To estimate the systematics of true pyrite concentration in the eastern tropical North Atlantic, we summed the count rates of the pixels of each XANES-verified true pyrite particle, converted to μg Fe with the XRF standard, and divided by the equivalent volume that was filtered through the mapped area to derive a pyrite concentration in the water column. This is a lower bound estimate of true pyrite concentration, since our criteria may underestimate the number of pyrite particles present, and thick particles will be underweighed because of beam penetration depth errors.

2.6. Quantification of average oxidation state from chemical-species maps

The area-normalized counts of each chemical species were determined by summing the counts from all pixels in each chemical-species map channel (background, pyrite, Fe(II)-containing species, Fe(III) species) and normalizing by area mapped. The area-normalized counts of each chemical species (including background) of process blank samples were subtracted from the samples, and blank-subtracted counts were then converted to μg Fe using the XRF thin film standards. For marine suspended particles, the blank QMA filters contributed most of the background counts in the sample chemical-species maps, probably due to scatter from the quartz fibers that make up the filter. Blank QMA filters also contained an average of 172 ± 26 ng Fe/cm^2, of which 78% was in Fe(II) form, but this was a small fraction of sample iron, whose loading ranged from 22–1200 μg/cm^2. The iron content of blank polycarbonate filters was negligible.

Because most of the counts in the pyrite channel are due to non-sulfidic Fe(II) for marine and aerosol samples, we add the counts in the pyrite channel to the Fe(II)-compound fraction and quantify total Fe(II)-containing species. Total Fe is the sum of the pyrite, Fe(II)-compound, and Fe(III)-compound channels. The average oxidation state from chemical-species mapping is simply the fraction of total Fe in the Fe(III) channel.

Most of the particles appearing in the pyrite channel of the chemical-species map of SIRENA sediments were

Table 2
Fe-bearing model compounds used in linear combination fits. The fraction of Fe(III), Fe(II), and sulfide attributed to each compound by the chemical species mapping parameters chosen is listed, as well as the equivalent oxidation state calculated from these fractions. Italicized values are false positives. For comparison, estimated oxidation states from a self-calibrating method based on the energies of the main edge relative to the pre-edge (Marcus et al., 2008) and from chemical formulae are also given.

Mineral	Mineralogical classification	Abbrev.	Chemical formula	Chemical-species mapping				Self-cal. method	Chemical formula
				Sulfide fraction	Fe(II) fraction	Fe(III) fraction	Oxidation state	Oxidation state	Oxidation state
Fe foil	Metal	Foil	Fe^{0}	*0.646*	*0.248*	*0.040*	1.9	2.06	0
Fe sulfides									
FeS	Sulfide	FeS	$Fe^{2+}S$	0.957	*0.126*	0.000	2.2	1.62	2
Pyrite	Sulfide	Pyr	$Fe^{2+}S_2$	1.000	0.000	0.000	2.0	2.11	2
Pyrrhotite	Sulfide	Prh	$Fe_7^{2+}S_8$	0.903	*0.189*	0.000	2.2	2.06	2
Fe(II)-containing minerals									
Almandine	Silicate–Fe–Al garnet	Alm	$Fe_3^{2+}Al_2Si_3O_{12}$	0.000	1.153	0.000	2.31	2.15	2
Augite	Silicate–clinopyroxene	Aug	$(Ca,Na)(Mg,Fe^{2+},Al,Fe^{3+},Ti)[(Si,Al)_2O_6]$	*0.144*	0.776	0.069	2.05	2.08	2/3 mix
Biotite	Silicate–mica	Bt	$KMg_{2.5}Fe^{2+}{}_{0.5}AlSi_3O_{10}(OH)_{1.75}F_{0.25}$	0.000	1.000	0.000	2.00	2.22	2
Fayalite60 (Fo40)	Silicate–olivine	Fay	$Fe_2^{2+}SiO_4$–Mg_2SiO_4	*0.097*	0.981	0.000	2.16	2.18	2
Ferrosilite	Silicate–orthopyroxene	Fsil	$Fe^{2+}MgSi_2O_6$	*0.121*	0.886	0.000	2.01	1.97	2
Seafloor basalt glass	Silicate–glass	Gla	N/A	*0.433*	0.603	0.000	2.07	1.99	N/A
Hornblende	Silicate-Amphibole	Hb	$(Ca,Na)_{2\text{-}3}(Mg,Fe,Al)_5(Al,Si)_8O_{22}(OH,F)_2$	*0.042*	0.615	0.343	2.34	2.51	2/3 mix
Hypersthene	Silicate–orthopyroxene	Hyp	$Mg^{2+},Fe^{2+}SiO_3$	*0.176*	0.880	0.000	2.11	1.94	2
Ilmenite	Oxide–Ti oxide/spinel	Ilm	$Fe^{2+}TiO_3$	*0.135*	0.445	*0.413*	2.40	2.14	2
Iron sulfate	Sulfate salt	SO4	$Fe^{2+}SO_4$	*0.000*	1.035	0.000	2.07	2.43	2
Magnetite	Oxide–spinel	Mgn	$Fe_2^{3+}Fe^{2+}O_4$	*0.089*	0.364	0.572	2.62	2.51	2.67
Pigeonite	Silicate-clinopyroxene	Pig	$Mg_{1.35}Fe^{2+}{}_{0.55}Ca_{0.1}Si_2O_6$	*0.107*	0.721	*0.158*	2.13	2.05	2
Ripidolite (CCa-2)	Silicate–chlorite	Chl	$(Mg,Fe^{2+})_5Al(Si_3Al)O_{10}(OH)_8$	*0.004*	0.932	0.062	2.06	2.42	2
Siderite	Carbonate	Sid	$Fe^{2+}CO_3$	0.000	1.105	0.000	2.2	2.16	2
Vivianite	Phosphate	Viv	$Fe_3^{2+}(PO_4)_2{\cdot}8H_2O$	*0.000*	0.867	0.106	2.05	2.35	2
Fe(III) species									
Aegirine powder avg.	Silicate–clinopyroxene	Aeg	$NaFe^{3+}(Si_2O_6)$	*0.000*	0.322	0.670	2.65	2.68	3
Akaganeite	Oxide-oxyhydroxide	Aka	$Fe^{3+}O(OH,Cl)$	*0.000*	0.052	0.969	3.01	3.04	3
Andradite	Silicate–Ca–Fe garnet	And	$Ca_3Fe_2^{3+}Si_3O_{12}$	0.000	0.000	0.900	2.70	3.27	3
Biogenic oxide	Oxide-oxyhydroxide	Box	N/A	*0.013*	0.156	0.828	2.82	2.77	3
Ca montmorillonite (STx-1)	Aluminosilicate clay	STx	N/A	0.000	0.000	0.931	2.79	3.22	3
Fe alginate	Organic complex	Alg	$Fe\text{-}(C_6H_8O_6)_n$	*0.015*	0.293	0.690	2.69	2.81	3
Fe dextran	Organic complex	Dex	$Fe\text{-}H(C_6H_{10}O_5)_xOH$	*0.008*	0.263	0.748	2.79	2.87	3
Ferrihydrite (2-line)	Oxide-oxyhydroxide	Fh2L	$Fe_5^{3+}HO_8{\cdot}4H_2O$ approx.	0.000	0.000	1.000	3.00	3.01	3
Ferrihydrite (6-line)	Oxide-oxyhydroxide	Fh6L	$Fe_5^{3+}HO_8{\cdot}4H_2O$ approx.	*0.010*	0.000	0.965	2.92	3.02	3
Ferrosmectite	Aluminosilicate clay	Smec	N/A	*0.009*	0.000	0.989	2.99	3.13	3
Goethite	Oxide-hydroxide	Gt	$\alpha\text{-}Fe^{3+}O(OH)$	0.000	*0.001*	1.017	3.05	3.07	3
Hematite	Oxide	Ht	$Fe_2^{3+}O_3$	0.000	*0.007*	1.021	3.08	3.07	3
Illite (IMt-1)	Aluminosilicate clay	Ill	$(K,H_3O)(Al,Mg,Fe)_2(Si,Al)_4O_{10}[(OH)_2,(H_2O)]$	0.000	*0.166*	0.845	2.87	2.78	3
Lepidocrocite	Oxide-oxyhydroxide	Lep	$\gamma\text{-}Fe^{3+}O(OH)$	*0.000*	0.000	0.974	2.92	3.07	3
Maghemite	Oxide–spinel	Mgh	$\gamma\text{-}Fe_2^{3+}O_3$	*0.026*	0.030	0.916	2.86	2.84	3
Nontronite	Silicate–clay	Non	$Na0.3Fe^{3+}2Si_3AlO_{10}(OH)_2{\cdot}4(H_2O)$	*0.000*	0.000	0.989	2.97	3.21	3

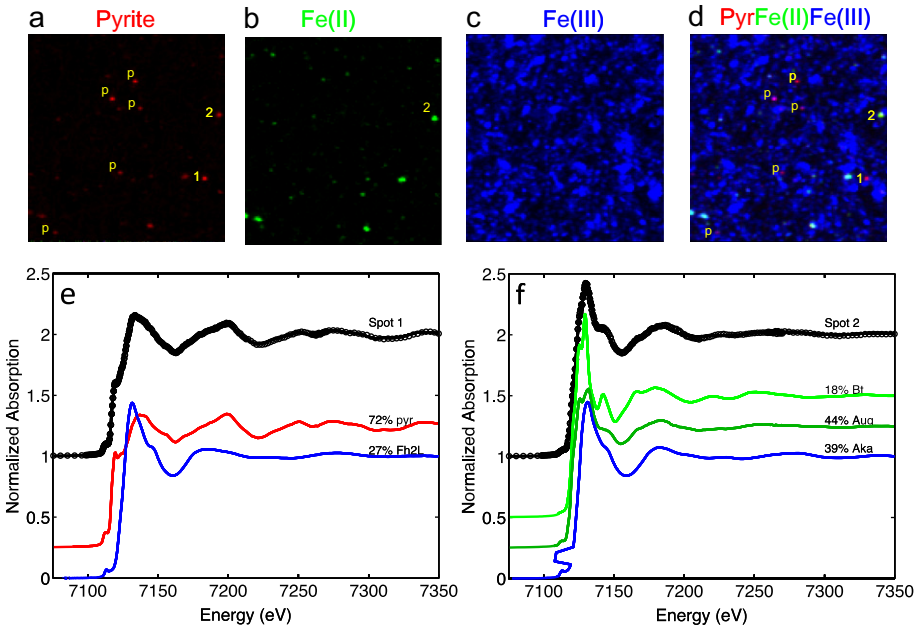

Fig. 3. Chemical species maps (a–d) and XANES spectra (e and f) from a 400 m suspended marine particulate sample from station 6 in the eastern tropical North Atlantic. Individual chemical species maps from the (a) pyrite (red), (b) Fe(II) (green), and (c) Fe(III) (blue) channels; (d) tricolor map showing all three species; XANES spectra for two particles denoted by the numbers 1 (e) and 2 (f) in the pyrite channel map. The best fit (black line) from linear combination of reference compounds to the data (circles) is shown with the reference compounds in the fits (colored lines). Each map is 500 μm × 500 μm with pixel size of 4 μm. The maximum color intensity of all three species has been set to 20,000cps. Typical maximum count rates are 150,000cps for Fe(III), 75,000 cps for (Fe(II), and 20,000cps for pyrite. The linearity of the color intensity for the pyrite channel is adjusted to accentuate lower counts. Additional particles categorized as "true" pyrite are denoted by p in the pyrite and tricolor maps.

confirmed by XANES to be true pyrite. There were too many pyrite particles in the chemical-species map of SIRENA sediments to count individually as was done for the water column samples. The abundance of pyrite, Fe(II)-containing species and Fe(III) species in the SIRENA sediments were estimated simply as the blank-corrected sum of counts in each respective channel. Because the Fe(II)-compound abundance was less than the pyrite abundance for this sample, the "false" pyrite signal due to non-sulfidic Fe(II)-containing species was likely a small percentage of the true pyrite signal. Nonetheless, the estimates of sedimentary pyrite concentrations are upper limits.

It should be noted that because samples were processed and stored dry at ambient temperature and atmosphere, the relative and absolute concentrations of Fe(II) that we report are a lower limit and represent the refractory Fe(II) only, as any organically complexed Fe(II) (Toner et al., 2009a) that might be present in the oxygen depleted zones would have oxidized by the time of our analysis.

2.7. μ-XANES data acquisition and linear combination fitting

To resolve the chemical speciation of particulate iron more finely than was possible from chemical species mapping, we collected extended micro-focused XANES (μ-XANES) spectra at the Fe K-edge from micron-scale Fe-rich spots from samples from station K2 in the Northwest Pacific and from the SIRENA cruise in the Eastern Tropical North Atlantic.

All μ-XANES data collection extended 300 eV above the Fe K-edge to aid in normalization and to pick up some EXAFS signal to better constrain the identification of unknown Fe-rich spots. A reproducible glitch in the monochromator at 7263.42 eV was used as an internal energy calibration. Extended μ-XANES spectra were collected from 7010–7414 eV, with 0.5 eV step sizes in the XANES region (7095–7140 eV) and near the monochromator glitch (7255–7275 eV), and coarser step sizes (1, 2, 5 eV) in the extended region (7140–7414 eV). The incident beam spot size was adjusted depending on the intensity of the particle count rate, but was typically 12 μm × 4 μm. Spectra were corrected for detector deadtime and energy drift, the pre-edge background was removed, and spectra were normalized before fitting.

XANES spectra of iron-rich micron-scale particles were collected from four groups of samples: 102 particles from seven marine particulate samples from station K2 in the Northwest Pacific (group 1), 222 particles from 32 marine particulate samples from the eastern tropical North Atlantic (group 2), 28 particles from three aerosol samples from the eastern tropical North Atlantic (group 3), and 13 particles from one sediment sample from the Mauritanian margin (group 4). Typically, μ-XANES spectra of five to fifteen micron-scale Fe-rich particles were collected for each sample.

For samples from the Northwest Pacific (group 1), μ-XANES spectra were collected before we had the benefit of chemical species maps to guide spot selection, so the

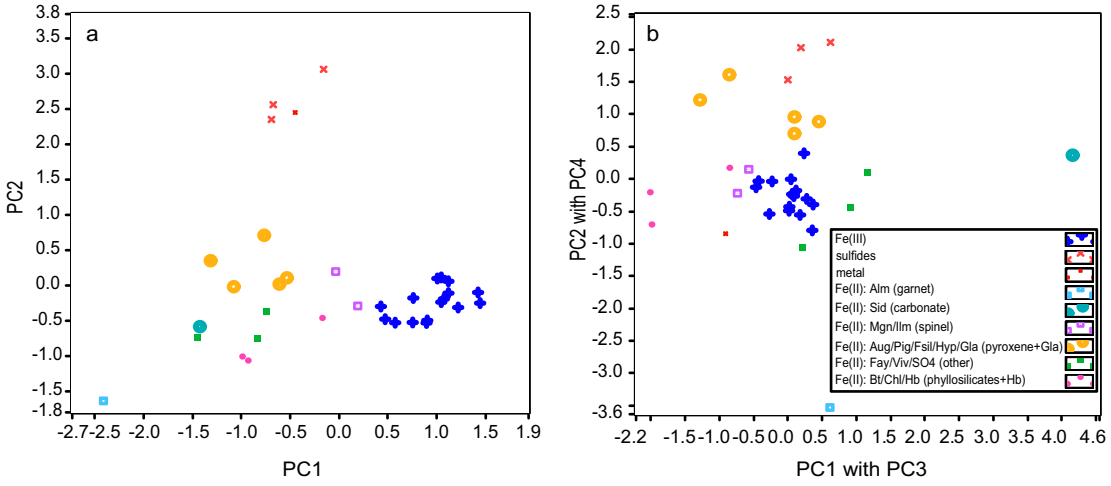

Fig. 4. Clustering of 35 model compounds by principal components analysis. Panels show the loadings of each model compound onto (a) principal components 1 and 2 (PC1, PC2), showing the separation into the three groups of references detected by chemical species mapping (Fe(III) species, Fe(II)-containing species, and sulfides), and (b) PC1 mixed with PC3 plotted against PC2 mixed with PC4. Identified clusters of Fe(II)-containing species are color-coded and stay together in both views. (For interpretation of the references to color in this figure legend, the reader is referred to the web version of this article.)

XANES data are a random selection of Fe species. For samples from the SIRENA cruise in the North Atlantic (groups 2–4), the chemical-species maps were used to guide the selection of Fe-rich spots on which to collect μ-XANES spectra. One of the goals of XANES spectra collection from the SIRENA samples was to verify the identification of pyrite and Fe(II) spots by the chemical-species mapping procedure, so we preferentially chose Fe(II) and pyrite spots identified by chemical-species mapping for XANES analysis. An analysis of the XANES dataset from the SIRENA samples would thus be biased towards the Fe(II) and pyrite species, even though these represented a small fraction of the total Fe (Figs. 5 and 6).

A library of extended XANES spectra of 35 Fe-containing model compounds (Table 2) maintained at beamline 10.3.2 was used to fit each sample spectrum. These model compounds represented a range of Fe(III) and refractory Fe(II) oxides, silicates, carbonates, and sulfides that might be found in suspended marine particles, sediments, and aerosols. Fe metal was also included to account for occasional contamination from metal dust.

Some of these model compounds exhibited significant similarities in their spectral features. Using software available at beamline 10.3.2, we performed principal component analysis (PCA) on the 35 model compounds to determine which model compounds group together based on spectral features. We selected the first six principal components, and used an experimental viewer program (not yet part of the on-line collection) that allowed the visualization of how the XANES spectra clustered in an abstract PCA space

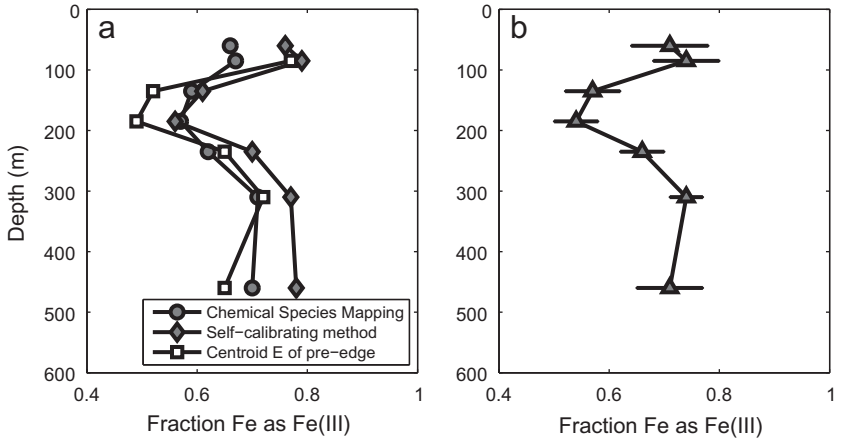

Fig. 5. Fraction of total particulate Fe in the Fe(III) oxidation state in 1–51 μm suspended particulate samples from station K2 in the Northwest Pacific. (a) Oxidation state determined by three methods: chemical species mapping (circles), bulk XAS "self-calibrating" method (Marcus et al., 2008) (diamonds), bulk XAS centroid method (Wilke et al., 2001)(squares). (b) Mean and standard deviation of the oxidation state of particulate iron at station K2 as determined by chemical species mapping, bulk XAS "self-calibrating", and the shifted bulk XAS centroid methods.

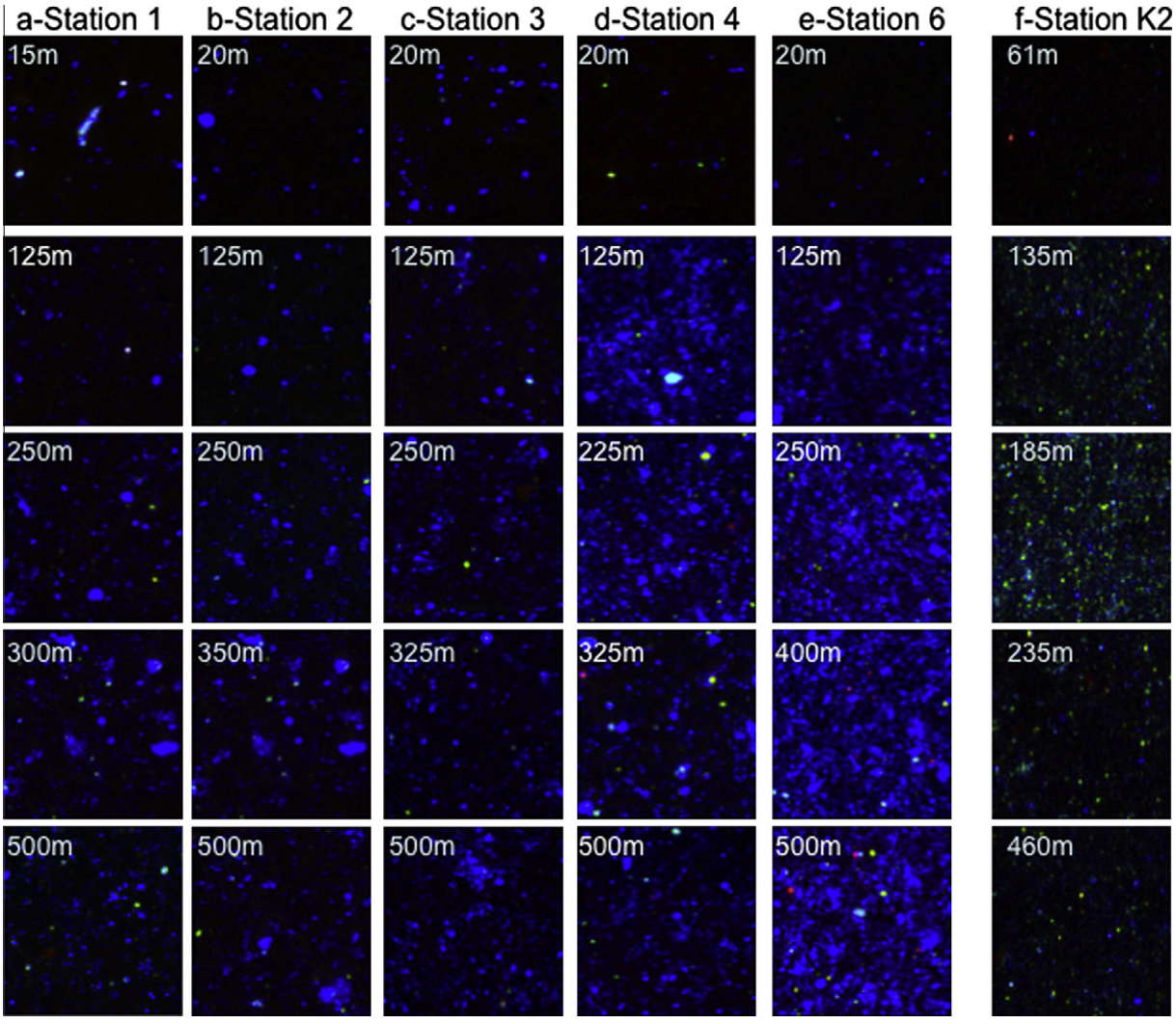

Fig. 6. Tricolor chemical species maps of 1–51 μm suspended particulates from five stations in the eastern tropical North Atlantic (a–e), and from station K2 in the Northwest Pacific (f) showing the spatial distribution of pyrite (red) Fe(II)-containing species (green) and Fe(III) species (blue). Depth of sample indicated. Color bars and mapping parameters as for Fig. 3.

whose coordinates are the loadings of the PCA abstract components. This program plots any combination of two PCA loadings against any other such combination, thus projecting the set of points (spectra) onto two dimensions with interactive control of the projection. The first principal component (PC0) defines the basic shape of an Fe K-edge XANES spectrum. Plotting the loadings of the reference compounds onto the second (PC1) and third (PC2) principal components easily separates the three main groups of references—Fe(III), Fe(II)-containing species, and sulfides—with PC1 separating on the basis of oxidation state, and PC2 pulling out the sulfides and Fe metal from the rest of the reference compounds (Fig. 4a). Within these three groups, clusters of reference compounds could be identified. Fig. 4b shows the effect of projecting onto a plane whose axes are weighted sums of the loadings of PC2 and PC4, and PC1 and PC3. If two or more points stayed together despite changes in the projection viewed, then they were considered to be adjacent in the multidimensional PCA space.

We found that the Fe(III) species could not easily be subdivided further, confirming the difficulty in separating Fe(III) species using XANES alone. Within the "sulfide" group, disordered FeS and pyrrhotite clustered together, but were distinct from pyrite and from Fe metal. Within the Fe(II)-containing species, six 1–5 compound "clusters" could be identified that remained together across several views, and that generally corresponded to mineralogical groups (Fig. 4a and b). The Fe(II) garnet almandine and the carbonate siderite were outliers and each formed a one compound "group"; the volcanic glass grouped most closely with the clino- and ortho-pyroxenes; a loose cluster consisting of olivine (fayalite), a sulfate salt ($FeSO_4$), and a phosphate mineral (vivianite) stayed closer to each other than to any other groups; the spinels (magnetite and ilmenite) clustered in the region between the Fe(III) species and the rest of the Fe(II)-containing species. Although mixed valence hornblende tended to cluster together with the spinels, we classified it together with the Fe(II) phyllosilicates biotite and chlorite, since we observed that sample spectra

were often equally well fit with hornblende compared to a mixture of an Fe(II) phyllosilicate and an Fe(III) species. The identification of the six clusters was not sensitive to the total number of principal components chosen.

For each sample XANES spectrum, we used a least squares fitting procedure that selected the best fits from among the 6545 unique non-negative combinations of the 35 model compounds taken three at a time. Because of the difficulty in using XANES to distinguish between Fe(III) species, the likely aging of Fe(III) species due to our preservation methods, and the different modes of spot selection in the Atlantic compared to Pacific samples, we report the mineralogy of refractory Fe(II)-containing species and sulfides only. The contributions of model compounds from linear combination fitting were summed for all particles within each of the four groups of samples (suspended marine particles from each basin, Saharan aerosol samples, and Mauritanian sediments). Summed Fe(II)-containing model compounds were grouped according to the six clusters identified in the principal component analysis.

It should be noted that the hundreds of XANES spectra we collected were nonetheless still a small fraction of all iron-rich particles in each sample, and quantification of the contribution of specific model compounds to the overall suspended particulate iron is difficult. Here, we are primarily concerned with comparing the assemblage of chemical species between groups of samples, and the prevalence of Fe(II)-containing mineral groups should be taken as a qualitative rather than quantitative description of mineral composition. For quantification of chemical species, we use chemical-species mapping.

3. RESULTS AND DISCUSSION

3.1. Evaluation of average oxidation state from chemical-species maps

We compared the average oxidation state of samples from station K2 from the Northwest Pacific determined by chemical-species mapping at microprobe beamline 10.3.2 to the average oxidation state determined from bulk XANES data collected previously on the same samples at SSRL beamline 7-3 (Lam and Bishop, 2008). Chemical-species maps are typically made over a 500 μm × 500 μm area, whereas the bulk XANES data integrate over the beam spot size of 2 mm × 15 mm. The average oxidation state of the bulk data was determined using two empirical methods: the first uses an empirical relationship between the absolute energy of the centroid of the pre-edge peak and the redox ratio of mixtures of octahedrally coordinated Fe minerals (Wilke et al., 2001; Lam and Bishop, 2008); the second method uses a "self-calibrating" method that relates the relative energy differences between the main edge and pre-edge features to the true oxidation states of model compounds (Marcus et al., 2008). The centroid method has the advantage of relying only on data taken at the foot of the edge, where absorbance is low and overabsorption is not a problem. The self-calibrating method has the advantage of being independent of absolute energy calibration of the beamline.

We found a systematic offset in the absolute partitioning of Fe(II) and Fe(III) species to higher Fe(III) using the centroid method (bulk) (Lam and Bishop, 2008) compared to the chemical-species mapping (microprobe) or self-calibrating (bulk) methods. This offset disappeared when a consistent Fe foil calibration of 7110.75 eV was used for all data, and the agreement between the three methods was quite good, all showing an influx of Fe(II) at around 135–185 m (Fig. 5). The agreement between the chemical-species mapping method on microprobe data collected at ALS beamline 10.3.2 and the centroid and self-calibrating methods on bulk data collected at SSRL beamline 7-3 suggests that the average oxidation state determined by chemical-species mapping is comparable to that determined by bulk XANES.

3.2. The distribution of particulate Fe species in the water column

Chemical-species maps show that suspended marine particulate Fe from the eastern tropical North Atlantic was overwhelmingly dominated by Fe(III) species (Figs. 6 and 7), accounting for an average of 90% of total iron. At very low total Fe concentrations at shallow depths, a few Fe(II)-containing particles at stations 1 and 4 lowered the % Fe(III) to 60–70% at the surface. Absolute Fe(II) concentrations were highest at station 6, the most coastal station, reaching 1.6nM at the total particulate Fe maximum at 200 m, but this still only accounted for 14% of total particulate Fe in that sample.

At station K2 in the Northwest Pacific, maximum absolute Fe(II) concentrations were similar (1.8 nM at 185 m) to the maximum at station 6 in the North Atlantic (Fig. 7), but the Fe(II)-containing species accounted for a significantly higher proportion of total iron overall (35%), reaching a maximum of 43% within this subsurface feature (Fig. 6).

The contrast in particulate iron concentrations and speciation between the Atlantic and the Pacific can be best demonstrated by comparing SIRENA station 3 in the eastern tropical North Atlantic with station K2 in the Northwest Pacific. Both stations are approximately 550 km from the nearest coast—the Mauritanian coast in the North Atlantic, and the Kuril-Kamchatka volcanic margin in the Northwest Pacific. Station 3 in the North Atlantic has almost threefold higher inventory of total particulate iron in the upper 500 m, with 7.09 mmol Fe/m^2 compared to 2.63 mmol Fe/m^2 in the Northwest Pacific station (Fig. 8, Table 1). The Fe(II) inventory at station K2 (0.95 mmol Fe(II)/m^2) was more than twice that of SIRENA station 3 (0.38 mmol (Fe(II)/m^2), and was in fact closest to the Fe(II) inventory at SIRENA station 6, only 140 km from the Mauritanian coast.

Pyrite particles were detected at stations 1, 4, and 6 in the eastern tropical North Atlantic (Figs. 6 and 9), but were not a significant contribution to total particulate iron (Figs. 7 and 9). The chemical species map and XANES spectra confirm at least one pyrite particle at 235 m in the Northwest Pacific as well (Fig. 6f). The apparent pyrite particle visible in the chemical map from station K2 at 61 m was likely due to contamination. While we did not take a

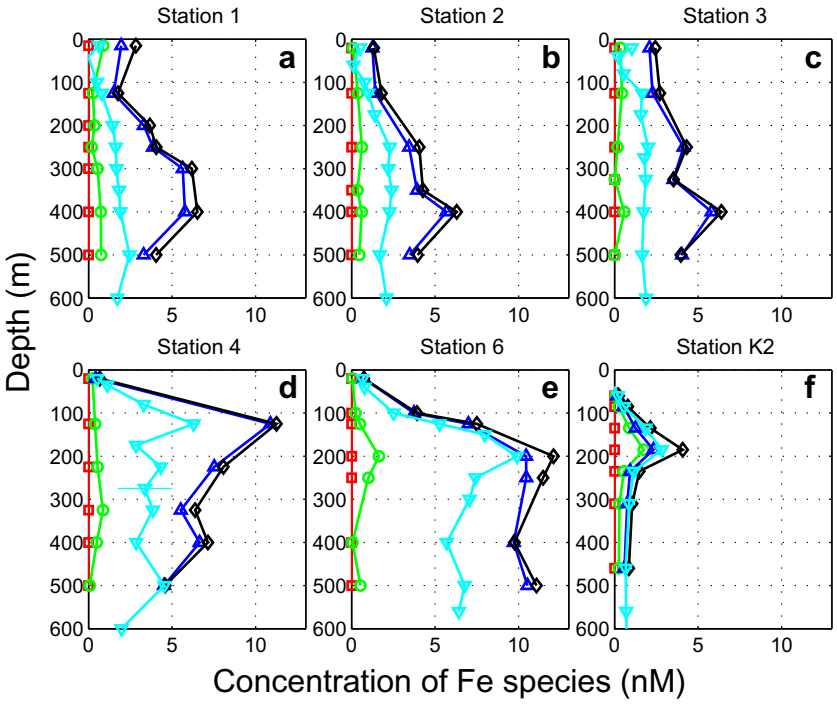

Fig. 7. Concentration of particulate Fe species in suspended marine particulate material from the eastern tropical North Atlantic (a–e) and the Northwest Pacific (f). Particulate iron species determined by chemical species mapping are pyrite (red squares), Fe(II)-containing species (green circles), Fe(III) species (dark blue upward triangles), and total particulate Fe (black diamonds). For comparison, acid-leachable particulate Fe determined by ICP-MS is plotted in cyan downward triangles. Note that pyrite concentrations are a lower limit (see Section 2.5). Error bars for acid-leachable particulate Fe are standard deviations of select repeat measurements. (For interpretation of the references to color in this figure legend, the reader is referred to the web version of this article.)

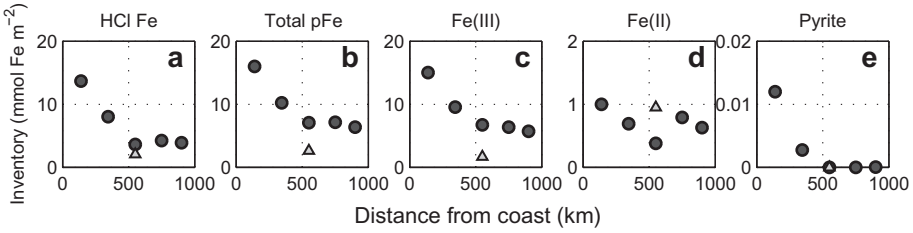

Fig. 8. Inventory of particulate iron species integrated over the upper 500 m as a function of distance from the coast. SIRENA samples are dark circles; K2 are light triangles. For SIRENA samples, station 1 is furthest from the coast.

XANES spectrum of this particle, it was co-located with anomalously high chromium count rates, suggesting that this was probably a stainless steel particle.

Acid-leachable Fe accounted for about half ($52 \pm 16\%$) of total Fe in the eastern tropical North Atlantic. Higher fractions (up to 85%) of acid-leachable Fe were found at the most coastal station (Fig. 9), suggesting that the coastal input of particulate Fe is most labile. In the Northwest Pacific, acid-leachable Fe accounted for a greater percentage of total Fe ($78 \pm 6.4\%$), despite its higher percentage of Fe(II). Concentrations and inventories of acid-leachable Fe (2.1 mmol/m^2) even exceeded those of Fe(III) (1.7 mmol/m^2) determined by chemical-species mapping, suggesting that this 0.6 N HCl leach must be accessing a portion of the Fe(II)-containing species in station K2 samples. Indeed, a cold, 24 h 1 N HCl leach was found to dissolve some Fe(II) minerals (Raiswell et al., 1994). The relatively low fraction of total Fe that was acid-leachable in the eastern tropical North Atlantic implies that the dominant Fe(III) species contain a highly refractory pool. A more detailed examination of the Fe(III) mineralogy of these samples by EXAFS spectroscopy, and/or a spectroscopic comparison of leached and unleached samples, may shed light on which phases are resistant to the acid leach.

3.3. Mineralogy of refractory Fe(II)-containing species

In all groups of samples, the most common group of refractory Fe(II)-containing compounds in fits were the phyllosilicates + Hb, which include the minerals biotite, chlorite, and hornblende (Hb) (Fig. 10). At station K2 in the Northwest Pacific, the spinels such as magnetite were the second most abundant group, whereas the pyroxenes + Gla were the second most abundant group in all

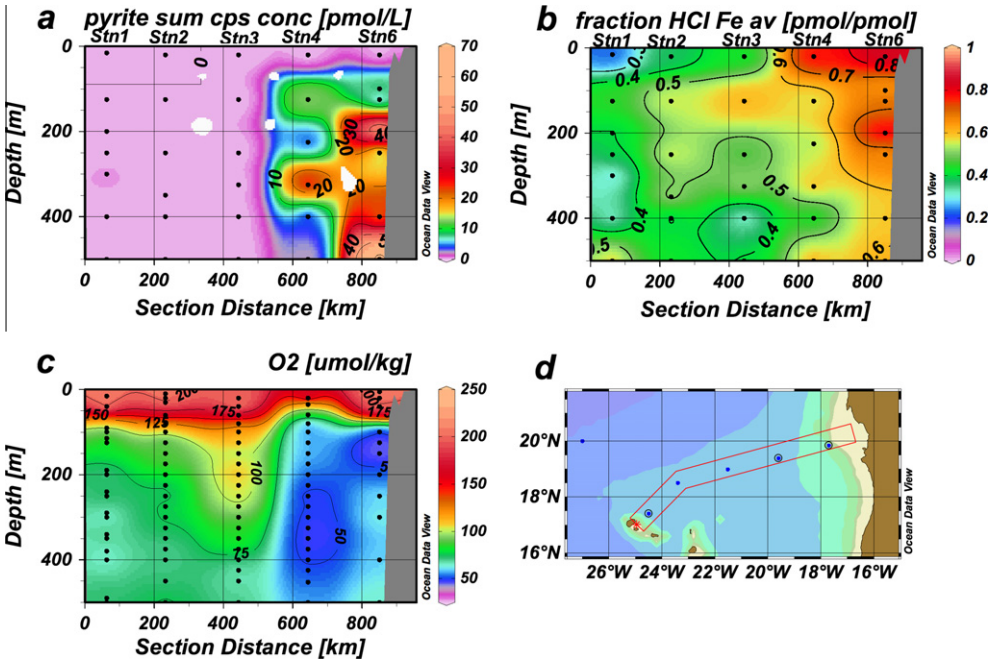

Fig. 9. Section plots from SIRENA showing (a) lower limit pyrite concentration, as determined by the count rates of the pixels in each confirmed pyrite particle (see Section 2.5), (b) fraction of total Fe that is acid-leachable, (c) oxygen concentration for CTD sensor, (d) map of cruise track. Oxygen data are from the oxygen sensor on the ship's CTD, which was calibrated on the cruise immediately prior to this one.

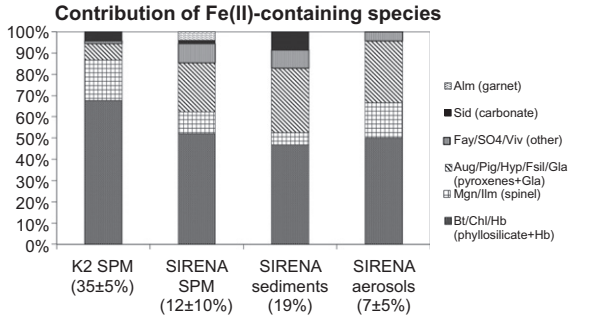

Fig. 10. Relative contribution of Fe(II)-containing model compounds in the four major groups of samples: K2 suspended particulate matter (SPM) from the Northwest Pacific, and SPM, sediments, and aerosols from the SIRENA project in the eastern tropical North Atlantic. The mean and standard deviation of the percentage contribution of Fe(II)-containing species to total Fe from chemical-species maps is indicated for each sample group.

SIRENA samples from the eastern tropical North Atlantic. Overall, the diversity of Fe(II)-containing minerals was higher in the SIRENA samples than the K2 samples.

Both the higher abundance and lower diversity of Fe(II)-containing minerals in the Northwest Pacific suspended particulate matter (SPM) is consistent with the Kuril-Kamchatka volcanic margin being the single dominant source of Fe(II)-containing minerals to the Northwest Pacific. In contrast, the higher diversity of Fe(II)-containing minerals in SIRENA samples suggests multiple sources. Indeed, Saharan dust can originate from many potential source regions in Africa (Chiapello et al., 1997), which could contribute to the mineral diversity. The overall similarity of the mineral assemblages in the aerosols, sediments, and SPM suggests that Saharan dust is the ultimate source of lithogenic material to the water column, whether by direct deposition as suspended particulate matter, or indirectly via deposition into the sediments and subsequent resuspension and lateral transport. In general, Fe(II) mineral assemblages of the sediments and aerosols are too similar to be able to use mineralogy to quantify their relative contributions to the water column. The exception to this is the presence of the mineral siderite in the SIRENA sediments and SPM, but not in the aerosols (Fig. 10), which, similar to pyrite discussed below, might be a qualitative tracer of a margin influence.

3.4. Pyrite: a unique tracer of lateral export from a highly productive margin

The dominant iron sulfide found in the water column was pyrite. We positively identified a total of 39 pyrite-containing particles at stations 1, 4, and 6 in SIRENA suspended marine particle samples from the eastern tropical North Atlantic (Figs. 5 and 8), with the highest number ($n = 29$) and concentration (64 pM) of pyrite at station 6, closest to shore. The intermediate stations 2 and 3 did not contain pyrite. While pyrite was always an insignificant fraction of total iron, its presence is indicative of oceanographic processes.

It is unlikely that pyrite observed in suspended marine particle samples formed authigenically in the bulk water column, since pyrite formation requires the absence of oxygen and water column dissolved oxygen levels in the North Atlantic transect never drop below 40 μmol/kg (Fig. 9).

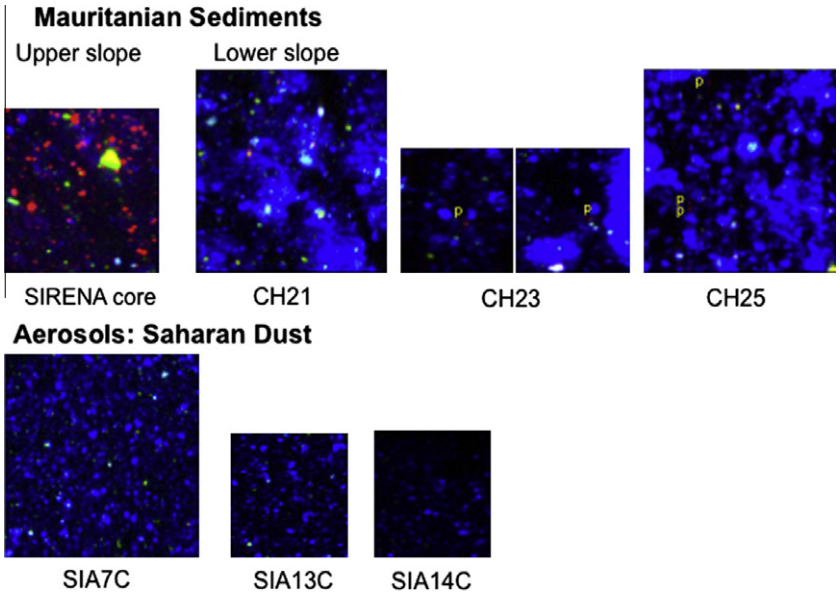

Fig. 11. Tricolor chemical species maps of Mauritanian sediments (top) and Saharan Dust aerosols (bottom). The map sizes are 300 μm × 300 μm for CH23, SIA13C2, SIA14C2; 400 μm × 400 μm for SIRENA sediments; 500 μm × 500 μm for CH21, CH25, and SIA7C2. Color bars and mapping parameters as for Fig. 3. For lower slope sediment samples, pyrite particles that were verified by XANES are noted with a "p". The red particle in CH21 was contamination from Fe metal.

While it is possible that micro-environments in water column particle aggregates might be more conducive to pyrite formation, it is more likely that the impingement of low oxygen waters on the highly productive Mauritanian continental margin leads to very shallow diagenetic formation of pyrite in continental margin sediments (Morse and Cornwell, 1987), which can then be resuspended and advected laterally into the water column. Indeed, chemical species mapping of the SIRENA core near-surface sediments collected from the Mauritanian margin shows abundant pure pyrite particles (Fig. 11), which we confirmed by XANES spectroscopy. The Mauritanian sediments were composed of up to 45% pyrite, 19% Fe(II)-containing species, and 36% Fe(III) species. For comparison, none of the aerosol samples contained any pyrite (Fig. 11). Like the suspended marine particles in this region, Saharan aerosols were dominated by Fe(III) species (87–97% Fe(III)). Pyrite nanoparticles from hydrothermal vents have recently been hypothesized to be transported long distances in the deep ocean (Yucel et al., 2011). As hydrothermal iron is unlikely to affect our suspended particulate samples, which were all collected at water depths shallower than 700 m, the pyrite that we observe is thus a unique tracer of resuspended continental margin sediments that have been advected laterally. Indeed, microscopic examination has shown that pyrite is the dominant iron sulfide mineral in sediments (Morse and Cornwell, 1987), consistent with the sediments being the source of pyrite to the water column.

An estimate of the geographical extent of the oxygen minimum zone from the World Ocean Atlas 2009 (WOA09) data (Garcia et al., 2010) explains the patchy observations of pyrite in the water column along our coastal to open ocean transect. The cruise transect was on the edge of the oxygen minimum tongue, and stations 2 and 3 fell outside the 85 μmol/kg isoline of the WOA09 dissolved oxygen concentration (Fig. 1a). CTD-derived oxygen profiles taken during the cruise confirmed that stations 2 and 3 had higher dissolved oxygen levels (Fig. 9). Pyrite was only present when water column oxygen concentrations were 70 μmol/kg or less (Fig. 12), conditions met in the subsurface at stations 1, 4, and 6.

Using an empirical pyrite oxidation rate law determined for a temperature of 25 °C (Williamson and Rimstidt, 1994), we calculate a rate of pyrite oxidation of 4.2×10^{-10} mol m^{-2} s^{-1} at an oxygen concentration of 70 μM and assumed pH of 8.1. Subsurface temperatures at the depth

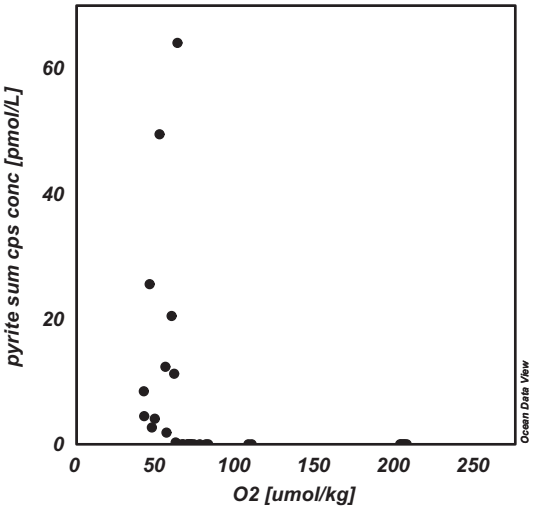

Fig. 12. Lower limit pyrite concentrations as a function of dissolved oxygen in the water a column for SIRENA samples.

of the continental margin are closer to 10–15 °C, which would further slow the rate of oxidation. Pyrite particles in the chemical species maps of suspended particles were typically a single pixel in size, putting their maximum diameter at 4 μm. The Stokes sinking velocities of 1 μm and 4 μm spherical pyrite particles in 25 °C seawater are 1.7×10^{-4} cm s^{-1} and 2.7×10^{-3} cm s^{-1}. In comparison, the zonal velocities at 200 m are up to 10 cm s^{-1} in this region (Stramma et al., 2005), leading to a transit time from the coast to the most offshore station 900 km away of at least 104 days. In that time, a 1 and 4 μm pyrite particle will have sunk 15 and 240 m, respectively, and 46% and 86% of the original 1 and 4 μm pyrite particles would have survived oxidation (Raiswell et al., 2009). At 200 μM dissolved oxygen, the 1 μm particle would be completely oxidized, but 64% of the 4 μm particle would have survived. Our calculations demonstrate that small, resuspended pyrite particles from the continental margin could easily survive the lateral transport to the water column hundreds of kilometers away in oxygen depleted waters.

The waters at stations 2 and 3 were likely more influenced by the more oxygenated descending limb of the Canary Current, whereas the waters at stations 1, 4, and 6 were within the oxygen minimum tongue. Core top sediments from box cores collected along the continental slope show a few particles of pyrite at two stations located within the oxygen minimum tongue, but not at a station north of the tongue (Figs. 1 and 9). These core-top sediments were collected between 1440 and 2700 m (Table 1), so are unlikely to be a source of pyrite to the upper water column. We interpret the pyrite in these core-top sediments to be from particles falling from the water column above rather than production within the sediments, since bottom waters at all three stations were well oxygenated. The distribution of pyrite in water column and core-top sediments suggests that the extent of pyrite in the water column likely maps onto that of the oxygen minimum tongue.

Examination of the other non-sulfidic minerals in the SIRENA core suggests that siderite could also be a tracer of resuspended continental margin sediments. Siderite is an Fe(II)-carbonate mineral that is also formed diagenetically in anoxic and low sulfate sediments (Mozley, 1989). While its presence in marine sediments was thought to be rare (Berner, 1971), it has nonetheless been found in modern high productivity anoxic marine sediments below the sulfate reduction zone (Haese et al., 1997). Siderite has a unique XANES spectrum that is easily distinguished from other minerals. It was relatively abundant in the SIRENA core XANES fits, did not appear in any of the fits to aerosol iron, and appeared, albeit rarely, in suspended marine particles from SIRENA stations 4 and 6 closest to the margin, suggesting authigenic formation of this carbonate mineral in the sediments and subsequent remobilization into the water column (Fig. 10). For samples from the eastern tropical North Atlantic, the higher abundance of pyrite in the sediments and water column, and the fact that we optimized our chemical-species mapping procedure to detect pyrite, make it an easier tracer to detect than siderite. In the Northwest Pacific, however, siderite was detected in two particles at 235 m compared to a single pyrite particle at 185 m. These depths were within the subsurface maximum in total iron that was linked to the continental margin (Lam and Bishop, 2008). Since both siderite and pyrite require anoxic sediments for their formation, and since the oxygen minimum zone is most intense north of station K2 towards the Kamchatka peninsula whereas the water column is well oxygenated by the Kuril Islands (cf. Fig. 1b), this implicates the Kamchatka peninsula as a source of these minerals.

At the energies used to make the chemical-species maps here, siderite was only detectable by sampling Fe(II) spots using XANES by trial and error. The siderite XANES spectrum is sufficiently unique that it should be possible to optimize the energies at which the input chemical-species maps are collected to uniquely identify siderite. Since both siderite and pyrite require anoxic conditions for their formation, the utility of these minerals as tracers for resuspended sediments from continental margins is likely restricted to highly productive margins adjacent to oxygen minimum zones.

3.5. Sources of iron to the eastern tropical North Atlantic

The lack of pyrite and increase in dissolved oxygen concentration in the water column at stations 2 and 3 suggest that the shortest distance from the coast may not necessarily represent the path of water masses to the SIRENA transect stations. Nonetheless, it is still clear that the inventories of total pFe, Fe(III) species, pyrite, and acid-leachable Fe decreased quickly with distance from the coast, supporting the idea that the margin is a source of these iron species and particulate iron in general to the water column (Fig. 8). There was no clear trend in the inventory of Fe(II)-containing species with distance from the coast, however, suggesting that atmospheric deposition may be a relatively more important source of Fe(II) to the water column than for Fe(III), for which the margin source is strong (Fig. 8).

4. CONCLUSIONS

We have shown that the average oxidation state by chemical-species mapping is comparable to that determined by standard bulk spectroscopy techniques. Chemical-species mapping has the added advantages of providing a visual representation of the extent and micron-scale spatial distribution of chemical species, and easily identifying minor species such as pyrite, that would never be identified by bulk techniques. In the case of the eastern tropical North Atlantic, pyrite was a unique tracer for the lateral transport of resuspended sediments from the continental margin into the water column. On a practical level, chemical-species mapping greatly increases the efficiency of beamtime use by providing a species "guide" for selecting which iron hotspots to target for more detailed analysis by XANES or EXAFS.

We found that the suspended marine particulate iron from the eastern tropical North Atlantic is dominated by Fe(III) species, whereas iron from station K2 in the Northwest Pacific has a much lower average oxidation state. Both the higher abundance and lower diversity of Fe(II)-contain-

ing minerals in the Northwest Pacific is consistent with the Kuril-Kamchatka volcanic margin being the single dominant source of Fe(II)-containing minerals to the Northwest Pacific. As the Kuril-Kamchatka margin is a volcanic arc formed from the subduction of the Pacific Plate, it is not surprising that this volcanic margin would be a better source of unweathered Fe(II)-containing minerals compared to the highly weathered, Precambrian rocks that form the Northwest African continent.

Studies of benthic iron flux from continental shelves have shown that reactive iron can be exported off the shelf in an iron shuttling process (Lyons and Severmann, 2006; Raiswell, 2011). In this process, dissolved Fe(II) from microbial reduction and dissolution of iron oxyhydroxides in sediments is mixed into the oxic water column by sediment resuspension events, re-oxidizes into nanoparticulate oxyhydroxides that can settle down and participate in the reduction—re-oxidation loop again, or be transported away from the margin. Here we have shown that the iron shuttle is not limited to nanoparticles. Indeed, our data suggest that the physical events that help to mix reductively dissolved Fe-rich porewaters into the oxic water column also serve to resuspend larger micron-scale sedimentary particles, where they too can be transported offshore.

Our data demonstrate that the speciation of Fe of suspended particulate matter in the open ocean reflects the lithology and sedimentary minerals of the adjacent continental margin. Since the solubility of particulate iron has been shown to be a function of its speciation, this may have implications for the bioavailability of particulate iron adjacent to passive compared to active continental margins.

ACKNOWLEDGEMENTS

This research was supported by NSF grant OCE-0726367 to P.J.L. The operations of the Advanced Light Source at Lawrence Berkeley National Laboratory are supported by the Director, Office of Science, Office of Basic Energy Sciences, US Department of Energy under contract number DE-AC02-05CH11231. The authors are grateful to Tim Eglinton and Dave Griffiths for providing core-top sediments from the NW African margin from the CHEETA cruise in 2007; the scientific and ship's crew of the R/V Oceanus for help at sea during the SIRENA cruise in 2008; Sirine Fakra, Hyojin Kim, Ralph Till, and John Swartz for assistance at the beamline; the many users at beamline 10.3.2 for contributing XANES spectra of Fe model compounds; Sirine Fakra for maintaining this database; Tracy Atwood for assistance in the laboratory; and Scot Birdwhistel l and the WHOI ICP facility for assistance on the ICP-MS. This manuscript was improved by the comments of Rob Raiswell and two anonymous reviewers.

REFERENCES

Berger C. J. M., Lippiatt S. M., Lawrence M. G. and Bruland K. W. (2008) Application of a chemical leach technique for estimating labile particulate aluminum, iron, and manganese in the Columbia River plume and coastal waters off Oregon and Washington. *J. Geophys. Res.* **113**, C00B01.

Berner R. A. (1971) *Principles of Chemical Sedimentology*. McGraw-Hill, New York.

Bishop J. K. B. and Wood T. J. (2008) Particulate matter chemistry and dynamics in the twilight zone at VERTIGO ALOHA and K2 sites. *Deep Sea Res. Part I: Oceanogr. Res. Pap.* **55**, 1684–1706.

Boyd P. W. and Ellwood M. J. (2010) The biogeochemical cycle of iron in the ocean. *Nat. Geosci.* **3**, 675–682.

Boyd P. W., Ibisanmi E., Sander S. G., Hunter K. A. and Jackson G. A. (2010) Remineralization of upper ocean particles: implications for iron biogeochemistry. *Limnol. Oceanogr.* **55**, 1271–1288.

Brown G. E. and Sturchio N. C. (2002) An overview of synchrotron radiation applications to low temperature geochemistry and environmental science. *Rev. Mineral. Geochem.* **49**, 1–115.

Buck C. S., Landing W. M., Resing J. A. and Measures C. I. (2010) The solubility and deposition of aerosol Fe and other trace elements in the North Atlantic Ocean: observations from the A16N CLIVAR/CO2 repeat hydrography section. *Mar. Chem.* **120**, 57–70.

Chiapello I., Bergametti G., Chatenet B., Bousquet P., Dulac F. and Soares E. S. (1997) Origins of African dust transported over the northeastern tropical Atlantic. *J. Geophys. Res.-Atmos.* **102**, 13701–13709.

Chrysochoou M., Fakra S. C., Marcus M. A., Moon D. H. and Dermatas D. (2009) Microstructural analyses of Cr(VI) speciation in Chromite Ore Processing Residue (COPR). *Environ. Sci. Technol.* **43**, 5461–5466.

Elrod V. A., Berelson W. M., Coale K. H. and Johnson K. S. (2004) The flux of iron from continental shelf sediments: a missing source for global budgets. *Geophys. Res. Lett.* **31**, L12307.

Frew R. D., Hutchins D. A., Nodder S., Sanudo-Wilhelmy S., Tovar-Sanchez A., Leblanc K., Hare C. E. and Boyd P. W. (2006) Particulate iron dynamics during FeCycle in subantarctic waters southeast of New Zealand. *Global Biogeochem. Cycles* **20**, GB1S93.

Garcia H. E., Locarnini R. A., Boyer T. P., Antonov J. I., Baranova O. K., Zweng M. M. and Johnson D. R. (2010) Dissolved oxygen, apparent oxygen utilization, and oxygen saturation. In *World Ocean Atlas 2009* (ed. S. Levitus). U.S. Government Printing Office, Washington, DC.

Haese R. R., Wallmann K., Dahmke A., Kretzmann U., Muller P. J. and Schulz H. D. (1997) Iron species determination to investigate early diagenetic reactivity in marine sediments. *Geochim. Cosmochim. Acta* **61**, 63–72.

Journet E., Desboeufs K. V., Caquineau S. and Colin J. L. (2008) Mineralogy as a critical factor of dust iron solubility. *Geophys. Res. Lett.* **35**, L07805.

Lam P. J. and Bishop J. K. B. (2008) The continental margin is a key source of iron to the HNLC North Pacific Ocean. *Geophys. Res. Lett.* **35**, L07608.

Lam P. J., Bishop J. K. B., Henning C. C., Marcus M. A., Waychunas G. A. and Fung I. Y. (2006) Wintertime phytoplankton bloom in the subarctic Pacific supported by continental margin iron. *Global Biogeochem. Cycles* **20**. doi:10.1029/2005GB002557.

Landing W. M. and Bruland K. W. (1987) The contrasting biogeochemistry of iron and manganese in the Pacific-Ocean. *Geochim. Cosmochim. Acta* **51**, 29–43.

Lyons T. W. and Severmann S. (2006) A critical look at iron paleoredox proxies: new insights from modern euxinic marine basins. *Geochim. Cosmochim. Acta* **70**, 5698–5722.

Manceau A., Marcus M. A., and Tamura N. (2002) Quantitative speciation of heavy metals in soils and sediments by synchrotron X-ray techniques, *Applications of Synchrotron Radiation in Low-Temperature Geochemistry and Environmental Sciences*. Mineralogical Society of America, Washington, DC.

Marcus M. A. (2010) X-ray photon-in/photon-out methods for chemical imaging. *Trends Anal. Chem.* **29**, 508–517.

Marcus M. A., MacDowell A. A., Celestre R., Manceau A., Miller T., Padmore H. A. and Sublett R. E. (2004) Beamline 10.3.2 at ALS: a hard X-ray microprobe for environmental and materials sciences. *J. Synchrotron Radiat.* **11**, 239–247.

Marcus M. A., Westphal A. J. and Fakra S. C. (2008) Classification of Fe-bearing species from K-edge XANES data using two-parameter correlation plots. *J. Synchrotron Radiat.* **15**, 463–468.

Moore J. K. and Braucher O. (2008) Sedimentary and mineral dust sources of dissolved iron to the world ocean. *Biogeosciences* **5**, 631–656.

Morse J. W. and Cornwell J. C. (1987) Analysis and distribution of iron sulfide minerals in recent anoxic marine sediments. *Mar. Chem.* **22**, 55–69.

Mozley P. S. (1989) Relation between depositional environment and the elemental composition of early diagenetic siderite. *Geology* **17**, 704–706.

Nodwell L. M. and Price N. M. (2001) Direct use of inorganic colloidal iron by marine mixotrophic phytoplankton. *Limnol. Oceanogr.* **46**, 765–777.

O'Day P. A., Rivera N., Root R. and Carroll S. A. (2004) X-ray absorption spectroscopic study of Fe reference compounds for the analysis of natural sediments. *Am. Mineral.* **89**, 572–585.

Ogliore R. C., Butterworth A. L., Fakra S. C., Gainsforth Z., Marcus M. A. and Westphal A. J. (2010) Comparison of the oxidation state of Fe in comet 81P/Wild 2 and chondritic-porous interplanetary dust particles. *Earth Planet. Sci. Lett.* **296**, 278–286.

Oram L. L., Strawn D. G., Marcus M. A., Fakra S. C. and M√∂ller G. (2008) Macro- and microscale investigation of selenium speciation in Blackfoot River, Idaho sediments. *Environ. Sci. Technol.* **42**, 6830–6836.

Pickering I. J., Prince R. C., Salt D. E. and George G. N. (2000) Quantitative, chemically specific imaging of selenium transformation in plants. *Proc. Nat. Acad. Sci. U.S.A.* **97**, 10717–10722.

Poulton S. W. and Raiswell R. (2005) Chemical and physical characteristics of iron oxides in riverine and glacial meltwater sediments. *Chem. Geol.* **218**, 203–221.

Raiswell R. (2011) Iceberg-hosted nanoparticulate Fe in the Southern Ocean: mineralogy, origin, dissolution kinetics and source of bioavailable Fe. *Deep Sea Res. Part II: Topical Stud. Oceanogr.* **58**, 1364–1375.

Raiswell R., Canfield D. E. and Berner R. A. (1994) A comparison of iron extraction methods for the determination of degree of pyritisation and the recognition of iron-limited pyrite formation. *Chem. Geol.* **111**, 101–110.

Raiswell R., Benning L. G., Davidson L., Tranter M. and Tulaczyk S. (2009) Schwertmannite in wet, acid, and oxic microenvironments beneath polar and polythermal glaciers. *Geology* **37**, 431–434.

Raiswell R., Vu H. P., Brinza L. and Benning L. G. (2010) The determination of labile Fe in ferrihydrite by ascorbic acid extraction: methodology, dissolution kinetics and loss of solubility with age and de-watering. *Chem. Geol.* **278**, 70–79.

Rich H. W. and Morel F. M. M. (1990) Availability of well-defined iron colloids to the marine diatom *Thalassiosira Weissflogii*. *Limnol. Oceanogr.* **35**, 652–662.

Schroth A. W., Crusius J., Sholkovitz E. R. and Bostick B. C. (2009) Iron solubility driven by speciation in dust sources to the ocean. *Nat. Geosci.* **2**, 337–340.

Schwertmann U. and Cornell R. M. (2000) *Iron Oxides in the Laboratory: Preparation and Characterization*. Wiley-VCH Verlag GmbH.

Sedwick P. N., Sholkovitz E. R. and Church T. M. (2007) Impact of anthropogenic combustion emissions on the fractional solubility of aerosol iron: evidence from the Sargasso Sea. *Geochem. Geophys. Geosyst.* **8**, Q10Q06.

Seibold E. and Berger W. H. (1993) *The Sea Floor: An Introduction to Marine Geology*. Springer-Verlag, Berlin.

Sholkovitz E. R., Sedwick P. N. and Church T. M. (2009) Influence of anthropogenic combustion emissions on the atmospheric deposition of soluble aerosol iron to the oceans: empirical estimates for island sites in the North Atlantic Ocean. *Geochim. Cosmochim. Acta* **73**, 3981–4003.

Stramma L., Huttl S. and Schafstall J. (2005) Water masses and currents in the upper tropical northeast Atlantic off northwest Africa. *J. Geophys. Res.-Oceans* **110**, C12006.

Sutton S. R., Bajt S., Delaney J., Schulze D. and Tokunaga T. (1995) Synchrotron X-Ray-fluorescence microprobe – Quantification and mapping of mixed-valence state samples using micro-xanes. *Rev. Sci. Instrum.* **66**, 1464–1467.

Tagliabue A., Bopp L. and Aumont O. (2009) Evaluating the importance of atmospheric and sedimentary iron sources to Southern Ocean biogeochemistry. *Geophys. Res. Lett.* **36**, L13601.

Toner B. M., Fakra S. C., Manganini S. J., Santelli C. M., Marcus M. A., Moffett J., Rouxel O., German C. R. and Edwards K. J. (2009a) Preservation of iron(II) by carbon-rich matrices in a hydrothermal plume. *Nat. Geosci.* **2**, 197–201.

Toner B. M., Santelli C. M., Marcus M. A., Wirth R., Chan C. S., McCollom T., Bach W. and Edwards K. J. (2009b) Biogenic iron oxyhydroxide formation at mid-ocean ridge hydrothermal vents: Juan de Fuca Ridge. *Geochim. Cosmochim. Acta* **73**, 388–403.

Wells M. L., Mayer L. M. and Guillard R. R. L. (1991) A chemical method for estimating the availability of iron to phytoplankton in seawater. *Mar. Chem.* **33**, 23–40.

Westphal A. J., Fakra S. C., Gainsforth Z., Marcus M. A., Ogliore R. C. and Butterworth A. L. (2009) Mixing fraction of inner solar system material in comet 81p/Wild2. *Astrophys. J.* **694**, 18–28.

Wilke M., Farges F., Petit P. E., Brown G. E. and Martin F. (2001) Oxidation state and coordination of Fe in minerals: an FeK-XANES spectroscopic study. *Am. Mineral.* **86**, 714–730.

Williamson M. A. and Rimstidt J. D. (1994) The kinetics and electrochemical rate-determining step of aqueous pyrite oxidation. *Geochim. Cosmochim. Acta* **58**, 5443–5454.

Yucel M., Gartman A., Chan C. S. and Luther G. W. (2011) Hydrothermal vents as a kinetically stable source of iron-sulphide-bearing nanoparticles to the ocean. *Nat. Geosci.* **4**, 367–371.

Associate editor: James McManus